Guideline to Series–Series Compensation Design and Bifurcation Mitigation in Multimodular IPT Systems

Calvin Riekerk, *Graduate Student Member, IEEE*, Jianning Dong, *Senior Member, IEEE*, and Pavol Bauer, *Senior Member, IEEE*

***Abstract*— The compensation and high-efficiency operation of the multimodular inductive power transfer (IPT) systems has been a challenge because of the inter- and cross-coupling between modular charging pads. This article analyzes the series–series (S–S) compensation and the associated bifurcation problem in multimodular IPT systems based on closed-form analytical modeling of the coupled circuits. From the analytical results, an improved compensation tuning method for multimodular systems is demonstrated. This improved compensation addresses the intercoupling between coils on the same side, in addition to the self-inductance of the charging pad. As a result, the system's efficiency improves while also saving an extra capacitor compared with other circuit-based decoupling methods. In addition, a design guideline based on the sum of the coupling coefficients including cross-coupling is derived to avoid bifurcation. The phase angle of the input impedance is studied under various scenarios, demonstrating the validity of the proposed design guideline. Experimental results on a downscaled prototype show that the improved compensation method enhances efficiency by more than 2% compared with scenarios where intercoupling is not compensated, and verification of the proposed bifurcation mitigation guideline.**

***Index Terms*— Bifurcation, cross-coupling, wireless power transfer (WPT).**

I. Introduction

CHARGING heavy-duty vehicles, such as electric buses, requires a high amount of power. This is especially the case when fast charging is used. Inductive power transfer (IPT) could make the charging progress significantly more convenient by eliminating physical contacts. IPT has risen in popularity in recent years [1]. There has been considerable success in pushing the research in IPT systems to power levels at 20 kW [2], [3], [4], [5] and above. However, high power levels pose challenges to the design of power electronics and charging pads, as they increase the current throughout the entire system. This makes it challenging to achieve high efficiency because of limited conductor areas and leakage field constraints.

Received 15 October 2024; revised 27 December 2024 and 3 March 2025; accepted 1 April 2025. Date of publication 9 April 2025; date of current version 21 January 2026. Recommended for publication by Associate Editor Ricardo Lizana. *(Corresponding author: Calvin Riekerk.)*

The authors are with the DC System, Energy Conversion and Storage (DCE&S) Group, Faculty of Electrical Engineering, Mathematics and Computer Science (EEMCS), Delft University of Technology, 2624 CP Delft, The Netherlands (e-mail: C.Riekerk@tudelft.nl; J.Dong-4@tudelft.nl; P.Bauer@tudelft.nl).

Color versions of one or more figures in this article are available at https://doi.org/10.1109/JESTPE.2025.3559240.

Digital Object Identifier 10.1109/JESTPE.2025.3559240

Multimodular systems provide a simple solution by paralleling multiple one-to-one IPT systems together [6], [7], [8], [9], [10]. In this way, it is unnecessary to put any resources into redesigning a new IPT system for a higher power level as would be mandatory for a large single-phase or three-phase system.

Compared with conventional one-to-one IPT systems, the multimodular system suffers from inter- and cross-coupling. Intercoupling refers to the coupling between charging pads on the same side, while cross-coupling refers to the coupling between the Tx and Rx side of charging pads from different modules. Both of them will affect the operation of the multimodular IPT system, hindering it from optimal operation at high efficiency, as elaborated as follows.

A. Intercoupling Between the Modules

Using multiple modules, it will result in multiple power transfer paths between each module instead of only between the Tx and Rx side. As a consequence, there will also be a path between charging pads on the same side due to intercoupling. Therefore, it will interfere with the power transfer efficiency between the Tx and Rx side [11], [12], [13].

Several decoupling methods have been developed. An extra capacitor in addition to the conventional S–S compensation capacitor is placed in series in the high-frequency ac link in [14], [15]. The value of this capacitor compensates for the intercoupling between modules, but this comes at the cost of an additional component in the circuit, therefore increasing the system size. This is especially important for high-power systems where the physical size of the capacitors is large as they have higher voltage and current ratings. Another circuit-based method is adding an extra capacitor in the T-branch between all the transmitters or receivers [16], [17], [18]. However, as mentioned before, the extra capacitor comes at the cost of an increased system size.

B. Bifurcation Due to Inter- and Cross-Coupling

Typically, a reasonably high coupling between the charging pads is desired to maximize the efficiency of the magnetic link. The bifurcation problem for conventional one-to-one IPT systems has been extensively studied in [19] and [20]. In contrast, the inter- and cross-coupling present in multimodular IPT systems introduce additional complexity to the analysis. However, the expression of critical coupling for a one-to-one

IPT system as given in [19] is not directly applicable to a multimodular IPT system. The added inter- and cross-coupling when multiple modules are deployed could potentially result in sending the system in bifurcation [21], [22]. This complicates system control and can lead to the loss of zero voltage switching (ZVS) in the H-bridge inverter, thereby increasing overall system losses [19], [20]. The consequences of the cross-coupling on the bifurcation limit for a three-phase system have been found in [23]. However, there is no closed-form solution for critical coupling that addresses cross-coupling.

To address the aforementioned challenges, an adequate analytical model is essential to model the effects of the inter- and cross-coupling. Li et al. [13] demonstrate that intercoupling introduces a circulating current, but their work does not illustrate its impact on power transfer efficiency. Similarly, Mai et al. [17] only explain how intercoupling is decoupled, without providing an expression for its effect on efficiency. Hossain et al. [11] analyze a modular IPT system consisting of two modules and derive an expression for the system's power transfer efficiency. However, extending this expression to systems with more modules makes it more unintuitive to follow.

Based on the aforementioned challenges and literature review, the following research gaps remain.

1) The current circuit-based decoupling methods all use an extra capacitor increasing the overall system size.

2) There is currently no closed-form expression taking into account the inter- and cross-coupling to determine the critical point of bifurcation. This makes it hard to design a multimodular IPT system that is bifurcation-free.

To fill the research gaps mentioned above, this article analytically models a quadruple multimodular IPT system. Using the closed-form equations derived from this analytical model, the impact of inter- and cross-coupling between charging pads on power transfer is evaluated. Based on the modeling effort and the evaluation, the following contributions are made.

1) An improved S–S compensation tuning method is demonstrated in a multimodular system.

2) A guideline on how to avoid bifurcation in a multimodular system is proposed.

3) Validation of the improved compensation method and bifurcation guideline is carried out on a downscaled multimodular IPT system.

This article is structured as follows. Section II describes the investigated multimodular IPT system. Section III presents the closed-form equations used to model the inter- and cross-coupling, along with the improved compensation tuning and bifurcation guidelines. In Section IV, a downscaled prototype is constructed to compare the improved tuning method with the conventional compensation tuning method in terms of efficiency and to verify the proposed bifurcation mitigation guideline. Finally, the conclusion is provided in Section V.

II. System Description

The schematic of an arbitrary paralleled multimodular IPT system is illustrated in Fig. 1. Here, L_i^q denotes the self-inductance of module i, where superscript q is either T (transmitter) or R (receiver). Similarly, M_{ij}^q represents the

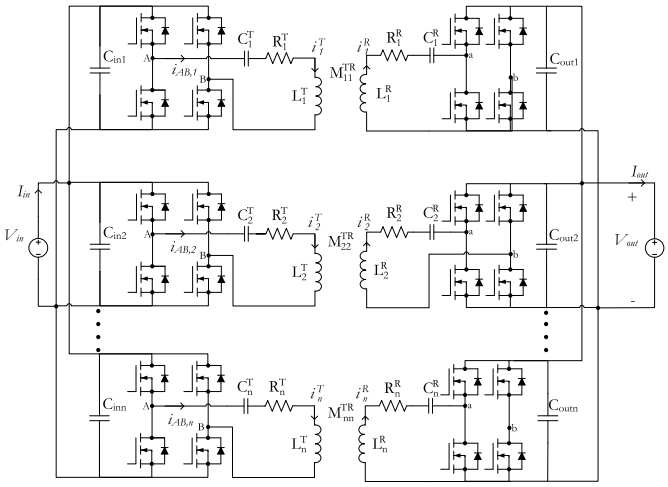

Fig. 1. Schematic of a multimodular IPT system.

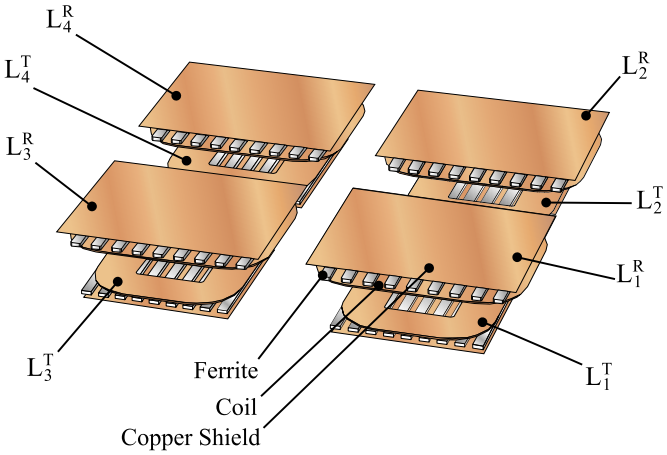

Fig. 2. Multimodular IPT system.

mutual inductance between modules i and j, with superscript q indicating T, R, or TR for coupling between two transmitters, two receivers, or a transmitter and a receiver, respectively. Synchronous rectification is used in the system to enhance the efficiency of the secondary-side power electronics. Furthermore, S–S compensation is used for its simple design, which contributes to low input resistance and ensures that current and compensation values remain independent of the load and coupling coefficient [20], [24], [25].

The investigated configuration of the four charging pad pairs is shown in Fig. 2 with its specifications detailed in Tables I and II. The charging pads are arranged in a 2 by 2 configuration, with a 10-cm separation to accommodate mechanical constraints due to the casing. Each charging pad consists of a copper shielding plate, ferrite bars of the material 3C95, and a litz wire winding.

III. Inter- and Cross-Coupling Modeling

The system described in Section II will be used to derive a model for the inter- and cross-coupling using closed-form equations. Using the equivalent model of Fig. 3 where $V_{n,1}^{\text{ref}}$ in (1) represents the reflected voltage of the receiver coils, $V_{n,2}^{\text{ref}}$

TABLE I
SPECIFICATIONS OF THE CHARGING PADS

Variable	Symbol	Unit	Primary	Secondary
Number of turns	N	-	13	11
Inner width of coil	W_{in}	cm	29.572	33.666
Inner length of coil	L_{in}	cm	42.56	55.654
Outer width of coil	W_{coil}	cm	76.98	65.82
Outer length of coil	L_{coil}	cm	63.988	87.81
Gap between turns	g_{turn}	mm	1.8	2.6
Ferrite width	W_{fe}	cm	4.32	4.32
Ferrite height	H_{fe}	cm	1.64	1.64
Ferrite length	Len_{fe}	cm	78.12	64.17
Number of ferrite bars	N_{fe}	-	9	9
Width of shielding	W_{sh}	cm	76.98	65.82
Length of shielding	L_{sh}	cm	63.988	87.81
Gap between coil and ferrite	g_{cf}	mm	0.30	3.24
Gap between ferrite and shielding	g_{fs}	mm	23.92	48.88
Thickness of shielding	t_{sh}	mm	1	1

TABLE II
INDUCTANCES OF THE MULTIMODULAR IPT SYSTEM

	L/M [μH]
$L_1^T = L_2^T = L_3^T = L_4^T$	169.11
$L_1^R = L_2^R = L_3^R = L_4^R$	154.23
$M_{11}^{TR} = M_{22}^{TR} = M_{33}^{TR} = M_{44}^{TR}$	54.423
$M_{13}^T = M_{24}^T$	0.62598
$M_{12}^R = M_{34}^R$	2.8960
$M_{13}^{TR} = M_{24}^{TR}$	0.48531
$M_{31}^{TR} = M_{42}^{TR}$	0.48062
$M_{14}^T = M_{23}^T$	0.15485
$M_{13}^R = M_{24}^R$	1.3338
$M_{12}^T = M_{34}^T$	4.7901
$M_{14}^{TR} = M_{23}^{TR}$	0.32460
$M_{41}^{TR} = M_{32}^{TR}$	0.32333
$M_{12}^{TR} = M_{43}^{TR}$	3.2818
$M_{21}^{TR} = M_{34}^{TR}$	3.2772
$M_{14}^R = M_{23}^R$	0.43974

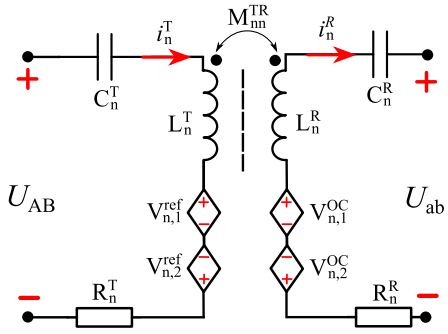

Fig. 3. AC equivalent model for the multimodular IPT system of a single module.

in (2) represents the reflected voltage of the other transmitter coils, $V_{n,1}^{OC}$ in (3) represents the open-circuit voltage of the transmitter coils, and $V_{n,2}^{OC}$ in (4) represents the open-circuit voltage of the other receiver coils. Subscripts x, y, and z denote the other three modules that are located close to module n. Applying KVL on the equivalent model in Fig. 3, the voltage equation describing the system's electrical behavior is given in (5). It is assumed that each of the four modules is supplied from the same dc voltage supply using four perfectly synchronized inverters as in [11] and [13]

$$V_{n,1}^{\text{ref}} = -j\omega\left(M_{nn}^{TR} I_n^R + M_{nx}^{TR} I_x^R + M_{ny}^{TR} I_y^R + M_{nz}^{TR} I_z^R\right) \tag{1}$$

$$V_{n,2}^{\text{ref}} = -j\omega\left(M_{nx}^{T} I_x^T + M_{ny}^{T} I_y^T + M_{nz}^{T} I_z^T\right) \tag{2}$$

$$V_{n,1}^{\text{OC}} = j\omega\left(M_{nn}^{TR} I_n^T + M_{xn}^{TR} I_x^T + M_{yn}^{TR} I_y^T + M_{zn}^{TR} I_z^T\right) \tag{3}$$

$$V_{n,2}^{\text{OC}} = j\omega\left(M_{nx}^{R} I_x^R + M_{ny}^{R} I_y^R + M_{nz}^{R} I_z^R\right) \tag{4}$$

$$\begin{bmatrix} U_{AB} \\ 0 \\ \vdots \\ U_{AB} \\ 0 \end{bmatrix} = \begin{bmatrix} A(1,2) & B \\ B^T & A(3,4) \end{bmatrix} \begin{bmatrix} I_1^T \\ I_1^R \\ \vdots \\ I_4^T \\ I_4^R \end{bmatrix} \tag{5}$$

where A and B matrices are given by

$$A(x,y) = \begin{bmatrix} Z_x^T & -cM_x^{TR} & cM_{xy}^T & -cM_{xy}^{TR} \\ -cM_x^{TR} & Z_x^R & -cM_{yx}^{TR} & cM_{xy}^R \\ cM_{xy}^T & -cM_{yx}^{TR} & Z_y^T & -cM_y^{TR} \\ -cM_{xy}^{TR} & cM_{xy}^R & cM_y^{TR} & Z_y^R \end{bmatrix} \tag{6}$$

$$B = \begin{bmatrix} cM_{13}^T & -cM_{13}^{TR} & cM_{14}^T & -cM_{14}^{TR} \\ -cM_{31}^{TR} & cM_{13}^R & -cM_{41}^{TR} & cM_{14}^R \\ cM_{23}^T & -cM_{23}^{TR} & cM_{24}^T & -cM_{24}^{TR} \\ -cM_{32}^{TR} & cM_{23}^R & -cM_{42}^{TR} & cM_{24}^R \end{bmatrix} \tag{7}$$

$$c = j\omega \tag{8}$$

where U_{AB} is the output ac voltage of the H-bridge inverter, I_n^T is the transmitting ac current through module n and, I_n^R is the receiving ac current through module n.

Assuming the self-inductances of the Tx and Rx pads are fixed, the Tx impedance can be described as

$$Z_n^T = R_n^T + j\left[\frac{(\omega^2 - \omega_0^2)L_n^T}{\omega}\right] \tag{9}$$

where R_n^T is the equivalent Tx resistance of module n, ω is the angular operating frequency, and ω_0 is the angular resonance frequency. The Rx impedance can be expressed as

$$Z_n^R = R_n^R + R_{\text{Lac}} + j\left[\frac{(\omega^2 - \omega_0^2)L_n^R}{\omega}\right] \tag{10}$$

where R_n^R is the equivalent Rx resistance of module n.

The equivalent load resistance is calculated as [26]

$$R_{\text{Lac}} = \frac{8}{\pi^2}\frac{V_{\text{out}}^2}{P_{\text{out}}} \tag{11}$$

where V_{out} is the output dc voltage and P_{out} is the output power for each module.

The reflected impedance on one of the Tx-side modules is given in (12), as shown at the bottom of the next page, where M_{nx}^T, M_{ny}^T, M_{nz}^T represent the intercoupled mutual inductances on the Tx side with module n. The terms Z_A–Z_D, shown in (13), represent the impedance of the coupled mutual inductances between the Tx side and the Rx charging pad of

module n. While Z_E–Z_H, as shown in (14), depicts the effect of the intercoupling between the Rx charging pads

$$\begin{bmatrix} Z_A \\ Z_B \\ Z_C \\ Z_D \end{bmatrix} = \begin{bmatrix} M_{nn}^{TR} & M_{nx}^{TR} & M_{ny}^{TR} & M_{nz}^{TR} \\ M_{xn}^{TR} & M_{xx}^{TR} & M_{xy}^{TR} & M_{xz}^{TR} \\ M_{yn}^{TR} & M_{yx}^{TR} & M_{yy}^{TR} & M_{yz}^{TR} \\ M_{zn}^{TR} & M_{zx}^{TR} & M_{zy}^{TR} & M_{zz}^{TR} \end{bmatrix} \begin{bmatrix} M_{nn}^{TR} \\ M_{nx}^{TR} \\ M_{ny}^{TR} \\ M_{nz}^{TR} \end{bmatrix} \tag{13}$$

$$\begin{bmatrix} Z_E \\ Z_F \\ Z_G \\ Z_H \end{bmatrix} = \begin{bmatrix} 0 & M_{nx}^{R} & M_{ny}^{R} & M_{nz}^{R} \\ M_{nx}^{R} & 0 & M_{xy}^{R} & M_{xz}^{R} \\ M_{ny}^{R} & M_{ny}^{R} & 0 & M_{yz}^{R} \\ M_{nz}^{R} & M_{xz}^{R} & M_{yz}^{R} & 0 \end{bmatrix} \begin{bmatrix} M_{nn}^{TR} \\ M_{nx}^{TR} \\ M_{ny}^{TR} \\ M_{nz}^{TR} \end{bmatrix}. \tag{14}$$

The power transfer efficiency can be modeled using the equivalent load resistance (11), reflected impedance (12), and equivalent series resistances at the Tx and Rx sides as

$$\eta_{pt} = \frac{Re\left(Z_n^{\text{ref}}\right)}{Re\left(Z_n^{\text{ref}}\right) + R_n^T} \frac{R_{\text{Lac}}}{R_{\text{Lac}} + R_n^R}. \tag{15}$$

Equations (11)–(15) can be used when it is assumed that the current distribution at all the Tx and Rx modules is even provided that the ratio between the main coupling and inter- and cross-coupling is sufficiently high. The reflected impedance in (12) could increase compared with a one-to-one IPT system because of the additional mutual inductances due to the cross-coupling. This looks beneficial at first glance as it could improve the power transfer efficiency of a multimodular IPT system. However, impedances Z_E–Z_H caused by the intercoupling on the Rx side negatively impact the real part of the reflected impedance in (12), thereby reducing the power transfer efficiency as shown in (15). Furthermore, (12) indicates that the intercoupling caused at the Tx side generates additional reactive power compared with the reflected impedance of a conventional one-to-one IPT system, leading to additional losses.

A. Improved Compensation Tuning Method for a Multimodular S–S Compensated IPT System

As presented in the above analysis, the intercoupling is negatively affecting the multimodular IPT system, and as a result, the loss will be increased as shown in (12) and (15). To overcome this issue, an improved tuning method is used for the compensation to suppress the intercoupling between the modules in addition to the self-inductance. An improvement can be made by tuning the already existing compensation capacitor. The capacitors should be tuned according to the following equation when S–S compensation is used:

$$C_n^k = \frac{1}{\omega_0^2 (L_n^k + M_{\text{int}})} \tag{16}$$

where

$$M_{\text{int}} = M_{nx}^k + M_{ny}^k + M_{nz}^k. \tag{17}$$

When the compensation is tuned this way, the portion of the reflected impedance affected by the intercoupling in (12) will be suppressed. This would be beneficial for the power transfer efficiency described in (15).

Compared with other reported circuit-based decoupling methods [14], [15], [16], [17], [18], the main contribution of the improved tuning method is that it eliminates the need to place an extra capacitor in the circuit in addition to the already existing compensation capacitors, which benefits the overall system size. This is particularly important for high-power applications, where component size increases with power.

B. Bifurcation Caused by the Cross-Coupling With Multiple Modules

The equivalent model in Fig. 3 shows that the cross-coupling increases both the reflected and open-circuit voltages which in turn affect the system's input impedance. The phase angle curve of the input impedance is used to determine whether the system is in bifurcation. When this happens, it results in multiple frequencies where the phase angle of the input impedance is equal to zero and, among those frequencies, one is the chosen resonance frequency [19], [20]. The inductive region is the zone where the phase angle of the system's input impedance is positive. However, multiple zero crossings may appear in the phase angle, making it harder to find and achieve ZVS [23]. Solving the imaginary part of the input impedance is necessary to determine whether the system's phase angle has multiple zero crossings. The imaginary part of the input impedance is given by

$$\Im(Z_{in}) = \frac{\left(\omega^2 - \omega_0^2\right) L_n^T}{\omega} + \omega(\Sigma M_3) - \frac{\omega^2 (\Sigma M)^2 \left(\frac{\left(\omega^2 - \omega_0^2\right) L_n^T N}{\omega} + \omega(\Sigma M_2) \right)}{R_{\text{Lac}}^2 + \left(\frac{\left(\omega^2 - \omega_0^2\right) L_n^T N}{\omega} + \omega(\Sigma M_2) \right)^2} \tag{18}$$

where the sums of the mutual inductances are given by

$$\Sigma M = M_{nn}^{TR} + M_{xn}^{TR} + M_{yn}^{TR} + M_{zn}^{TR} \tag{19}$$

$$\Sigma M_2 = M_{nx}^{R} + M_{ny}^{R} + M_{nz}^{R} \tag{20}$$

$$\Sigma M_3 = M_{nx}^{T} + M_{ny}^{T} + M_{nz}^{T}. \tag{21}$$

The ratio of the self-inductances between the Tx and Rx side is given by

$$N = \frac{L_n^R}{L_n^T}. \tag{22}$$

$$Z_n^{\text{ref}} = \frac{\omega_0^2}{Z_n^R} \left(Z_A + \frac{I_x^T}{I_n^T} Z_B + \frac{I_y^T}{I_n^T} Z_C + \frac{I_z^T}{I_n^T} Z_D - \frac{I_n^R}{I_n^T} Z_E - \frac{I_x^R}{I_n^T} Z_F - \frac{I_y^R}{I_n^T} Z_G - \frac{I_z^R}{I_n^T} Z_H \right) + j\omega_0 \left(\frac{I_x^T}{I_n^T} M_{nx}^T + \frac{I_y^T}{I_n^T} M_{ny}^T + \frac{I_z^T}{I_n^T} M_{nz}^T \right) \tag{12}$$

Considering the improved compensation tuning in Section III-A, this can be simplified by neglecting the mutual intercoupling as

$$\Im(Z_{in}) = \frac{\left(\omega^2 - \omega_0^2\right) L_n^T}{\omega} T_{ss} \tag{23}$$

where

$$T_{ss} = 1 - \frac{\omega^2 (\Sigma M)^2 N}{R_{\text{Lac}}^2 + \left(\frac{\left(\omega^2 - \omega_0^2\right) L_n^T N}{\omega}\right)^2}. \tag{24}$$

The sum of the mutual inductances between the Tx and Rx side is given by

$$\Sigma M = \Sigma k \sqrt{L_n^T L_n^R} \tag{25}$$

where

$$\Sigma k = k_{nn}^{TR} + k_{xn}^{TR} + k_{yn}^{TR} + k_{zn}^{TR}. \tag{26}$$

By substituting (25) into (24) and solving it, the following closed-form expression is obtained, specifying the critical sum of the coupling coefficients for module n, which results in bifurcation:

$$\Sigma k > \Sigma k_{\text{crit}} = \frac{R_{\text{Lac}}}{\omega_0 L_n^R}. \tag{27}$$

It is important to note that (27) can still be used under misaligned conditions, as long as the positions of the same side coils remain unchanged, being fixed on the vehicle or ground. Consequently, the intercoupling remains nearly constant when the coils are misaligned. However, the cross-coupling will vary similar to the coupling between the same module coils. As a result, the optimal equivalent ac load resistance will decrease in the same manner as the sum of the coupling in (26). Therefore, the proposed method remains applicable for misaligned conditions, provided that the change in the intercoupling remains minimal. To verify the closed-form expression in (27), the phase angle of the input impedance from the 5-kW IPT system described in Table I will be used. In Fig. 4 the phase angle of the input impedance is plotted for four different operating points: the sum of the coupling of Table II, 90% of the sum of the coupling, the critical coupling of the system, and when it is operated as a one-to-one IPT system. It is observed from Fig. 4 that multiple zero crossings appear when the coupling coefficient exceeds the critical limit which agrees with the expression in (27). In addition, it is illustrated that a bifurcation-free one-to-one IPT system can go into bifurcation when it is part of a multimodular IPT system.

Bifurcation can cause the system to lose ZVS which will reduce the overall efficiency of the IPT system. While such a guideline exists for one-to-one IPT systems [19], it does not apply to multimodular IPT systems due to the added inter- and cross-coupling from multiple modules. Previous work in [23] did not provide a closed-form solution, making it unintuitive to determine whether a multimodular IPT system is bifurcation-free. It is crucial for engineers to have a guideline as proposed in (27) to easily determine whether the system is bifurcation-free to prevent the loss of ZVS.

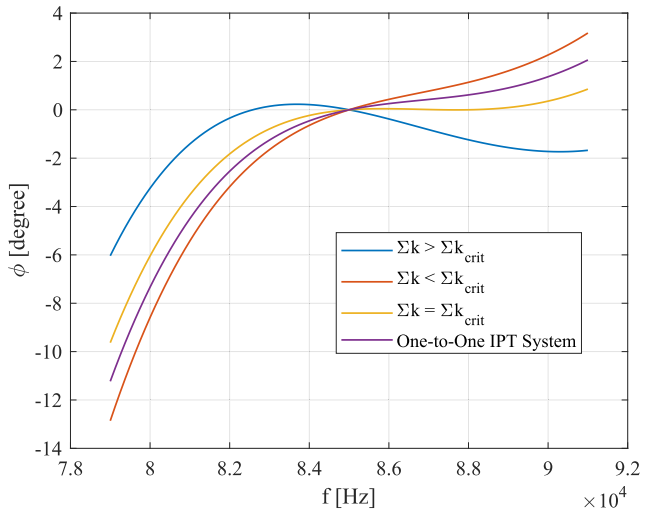

Fig. 4. Phase angle of the input impedance of a 50-kW module operated in parallel with three other modules, at 0.9 of its coupling, critical coupling, and as a one-to-one IPT system.

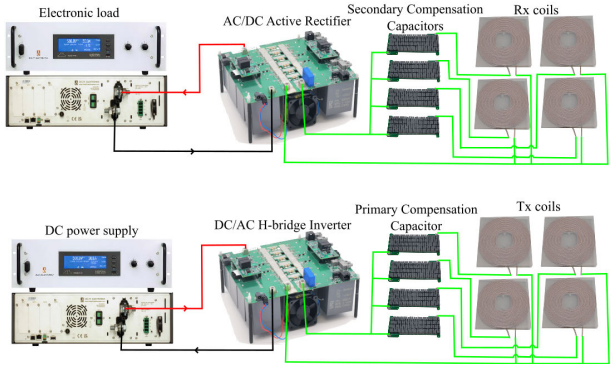

Fig. 5. Experimental setup of the downsized multimodular IPT system.

TABLE III
SPECIFICATIONS OF THE DOWNSCALED CHARGING PADS

Variable	Symbol	Unit	Primary/Secondary
Number of turns	N	-	20
Inner width of coil	W_{in}	mm	44.0
Inner length of coil	L_{in}	mm	44.0
Outer width of coil	W_{coil}	mm	146.0
Outer length of coil	L_{coil}	mm	146.0
Ferrite width	W_{fe}	mm	28
Ferrite height	H_{fe}	mm	4.1
Ferrite length	Len_{fe}	mm	129
Number of ferrite bars	N_{fe}	-	3
Gap between coil and ferrite	g_{cf}	mm	3.0

IV. EXPERIMENTAL VERIFICATION

A. Experimental Setup

To validate the theoretical analysis presented in Section III, a scaled-down version of the setup has been constructed, which includes H-bridge converters, compensation capacitors, and charging pads. Due to limited resources, the system has been downscaled. However, to ensure it remains representative, the system is scaled to achieve similar per-unit parameters and coupling coefficients.

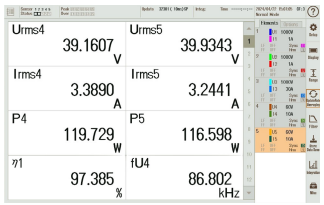

Fig. 6. Power transfer efficiency of a single module.

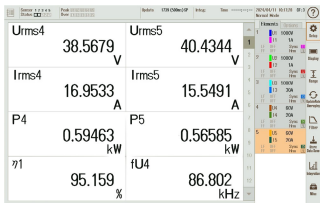

Fig. 7. Power transfer efficiency of the four modules using conventional compensation.

TABLE IV

MEASURED INDUCTANCES OF THE DOWN-SCALED MULTIMODULAR IPT SYSTEM

	L/M [μH]		M [μH]		M [μH]
L_1^T	59.8907	M_{12}^T	1.3928	M_{23}^T	0.3178
L_1^R	59.848	M_{12}^{TR}	1.1768	M_{23}^{TR}	0.2763
L_2^T	59.9738	M_{13}^T	0.8353	M_{24}^T	1.0298
L_2^R	60.5607	M_{13}^{TR}	0.5480	M_{24}^{TR}	0.5795
L_3^T	60.3181	M_{14}^T	0.3143	M_{32}^T	0.2833
L_3^R	58.0948	M_{14}^{TR}	0.328	M_{23}^R	0.2883
L_4^T	58.1566	M_{21}^{TR}	1.0118	M_{42}^{TR}	0.5730
L_4^R	59.1183	M_{12}^R	1.3323	M_{24}^R	1.0573
M_{11}^{TR}	17.5365	M_{31}^{TR}	0.5115	M_{34}^T	1.6283
M_{22}^{TR}	18.2194	M_{13}^R	0.8605	M_{34}^{TR}	1.2805
M_{33}^{TR}	17.5365	M_{41}^{TR}	0.2605	M_{43}^{TR}	1.116
M_{44}^{TR}	18.3743	M_{14}^R	0.3065	M_{34}^R	1.4118

TABLE V

MEASURED INDUCTANCES OF THE DOWN-SCALED MULTIMODULAR IPT SYSTEM MISALIGNED BY 25 MM

	L/M [μH]		M [μH]		M [μH]
L_1^T	58.610	M_{12}^T	1.4375	M_{23}^T	0.4
L_1^R	59.032	M_{12}^{TR}	0.8675	M_{23}^{TR}	0.565
L_2^T	59.059	M_{13}^T	0.9175	M_{24}^T	0.78
L_2^R	59.956	M_{13}^{TR}	0.87	M_{24}^{TR}	0.62
L_3^T	58.471	M_{14}^T	1.755	M_{32}^{TR}	0.38
L_3^R	59.268	M_{14}^{TR}	0.3325	M_{23}^R	0.38
L_4^T	58.217	M_{21}^{TR}	1.4775	M_{42}^{TR}	1.115
L_4^R	57.941	M_{12}^R	1.675	M_{24}^R	0.62
M_{11}^{TR}	12.9223	M_{31}^{TR}	0.5	M_{34}^T	1.203
M_{22}^{TR}	13.5323	M_{13}^R	0.6725	M_{34}^{TR}	0.91
M_{33}^{TR}	12.1208	M_{41}^{TR}	1.515	M_{43}^{TR}	1.645
M_{44}^{TR}	14.109	M_{14}^R	0.5925	M_{34}^R	1.535

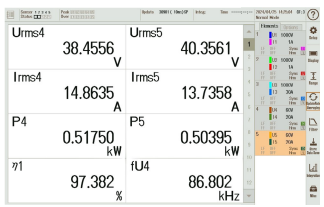

Fig. 8. Power transfer efficiency of the four modules using improved compensation.

Instead of each module having its own converter, a single H-bridge converter is used at both the Tx and Rx sides, as displayed in Fig. 5. The measurements of the downscaled coils are shown in Table III. The litz wire used has 600 strands with a strand diameter of 0.071 mm. The measured inductances during aligned condition are shown in Table IV, and Table V displays the inductances at an X and Y misalignment of 25 mm. These misalignment values are chosen so it would create the same drop in coupling coefficient as misalignment of 10 cm for the full power system. The film capacitors (EPCOS B32671L) are used. The first two capacitors are connected in series to ensure that the resonant capacitor is able to withstand the voltage. The values of the measured capacitances are presented in Table VI. Notably, the values for the improved capacitance are only used when all the four modules are connected in parallel.

TABLE VI

MEASURED COMPENSATION CAPACITANCES FOR BOTH CONVENTIONAL AND IMPROVED METHODS OF THE DOWN-SCALED MULTIMODULAR IPT SYSTEM

	Conventional C [nF]	Improved C [nF]
C_1^T	59.622	56.996
C_1^R	59.306	56.889
C_2^T	58.944	56.465
C_2^R	59.711	57.162
C_3^T	59.498	57.011
C_3^R	59.488	57.057
C_4^T	59.008	56.812
C_4^R	59.374	56.907

TABLE VII

AC POWER AND POWER TRANSFER EFFICIENCY MEASUREMENTS OF A SINGLE MODULE AND FOUR MODULES

		$P_{in,AC}$ [W]	$P_{out,AC}$ [W]	η [%]
Module 1	Aligned	147.90	142.22	96.159
	Misaligned	146.433	139.847	95.433
Module 2	Aligned	116.96	113.88	97.366
	Misaligned	156.383	149.664	95.703
Module 3	Aligned	119.729	116.60	97.385
	Misaligned	151.201	144.458	95.541
Module 4	Aligned	119.23	115.09	96.526
	Misaligned	149.743	142.571	95.211
Four modules (Conventional)	Aligned	594.63	565.85	95.159
	Misaligned	603.66	557.49	92.352
Four modules (Improved)	Aligned	517.50	503.95	97.382
	Misaligned	597.69	569.96	95.361

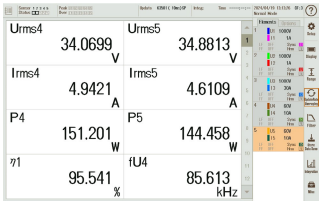

Fig. 9. Power transfer efficiency of a single module misaligned.

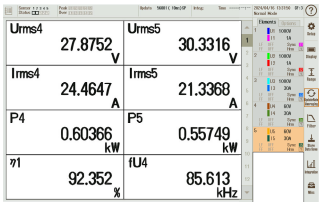

Fig. 10. Power transfer efficiency of the four modules using conventional compensation misaligned.

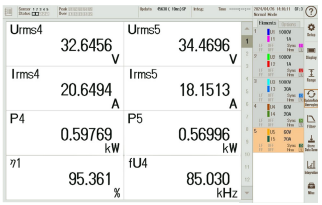

Fig. 11. Power transfer efficiency of the four modules misaligned using improved compensation.

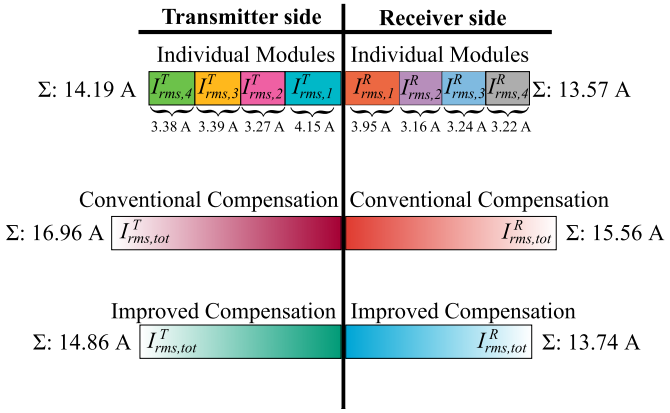

Fig. 12. Measured rms currents of the individual modules, four modules using the conventional compensation, and four modules using the improved compensation during aligned conditions.

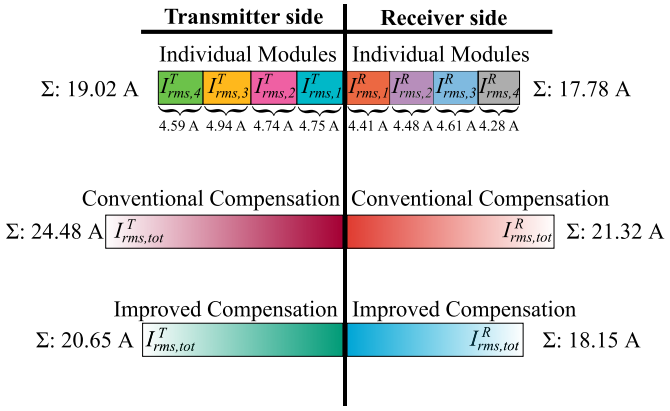

Fig. 13. Measured rms currents of the individual modules, four modules using the conventional compensation, and four modules using the improved compensation during misaligned conditions.

B. Improved Compensation Comparison

To illustrate the enhanced efficiency and reduction in circulating currents of the improved compensation tuning method, the power transfer efficiency and rms current are measured using a power analyzer (Yokogawa WT5000) and compared for the conventional and improved compensation methods at aligned and misaligned conditions using the setup described in Section IV-A. In addition, the efficiency of the individual modules is measured. In addition, the waveforms of the high-frequency ac voltage and currents of the improved compensation during both the aligned and misaligned conditions are measured. The measured efficiencies at aligned conditions are shown in Figs. 6, 7, and 8, with all the efficiencies compared in Table VII. The improved compensation tuning method demonstrates an increase of more than 2% over

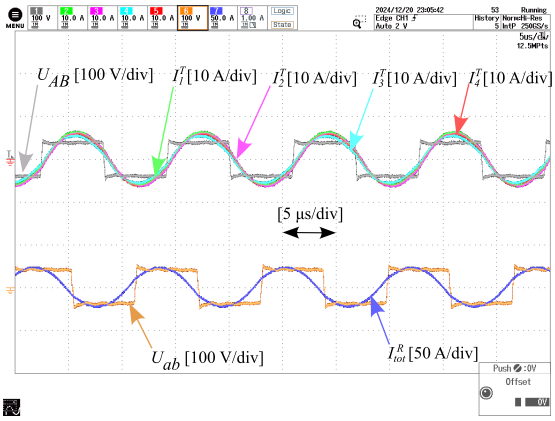

Fig. 14. Measured waveform using the improved compensation during aligned conditions.

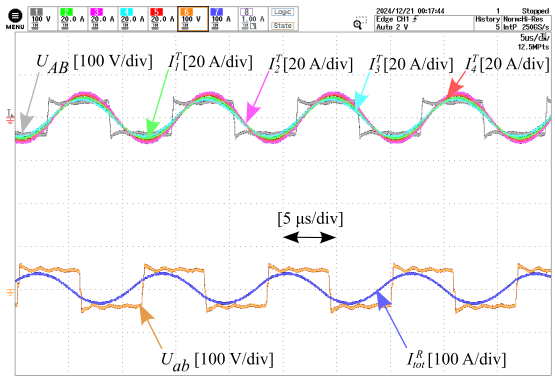

Fig. 15. Measured waveform using the improved compensation during misaligned conditions.

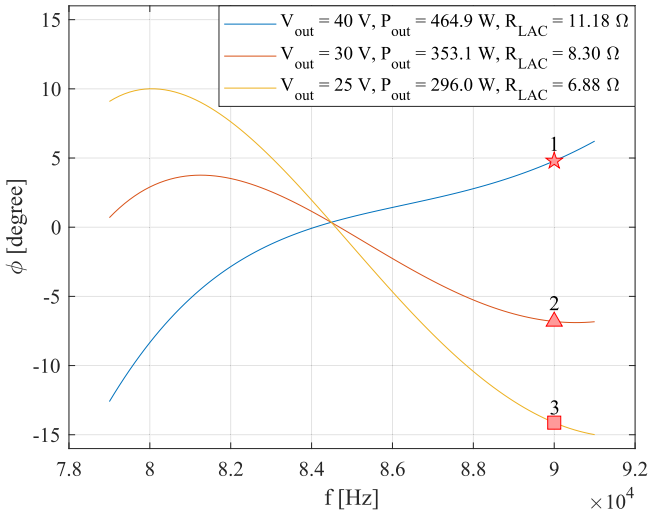

Fig. 16. Phase angle of the input impedance from the downscaled prototype for three different load conditions.

the conventional compensation tuning method, representing a significant upgrade, as discussed in Section III-A. An expected drop in efficiency is observed when the system operates during misalignment as shown in Figs. 9, 10, and 11. This trend is consistent across other modules as indicated in Table VII. The improved compensation tuning method enhances the efficiency

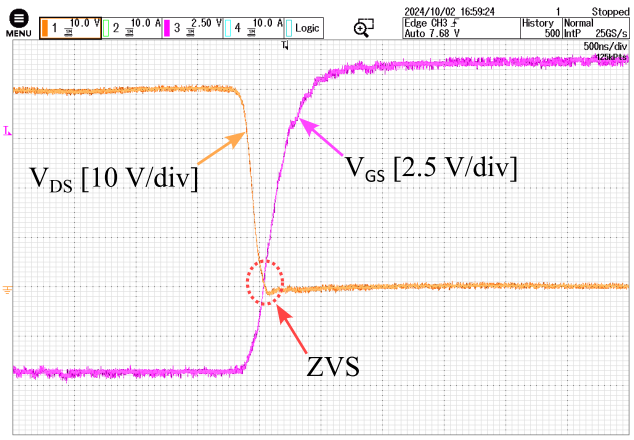

(a)

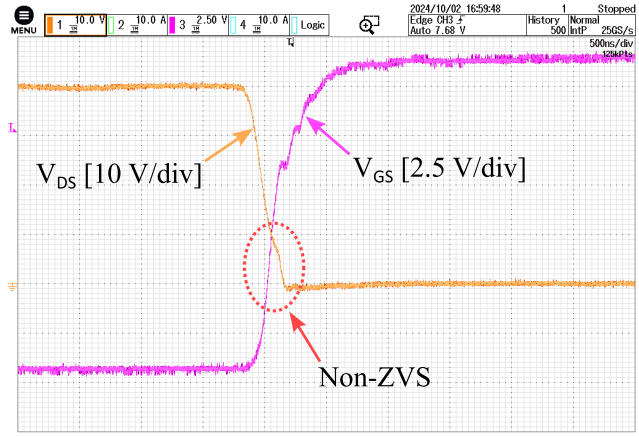

(b)

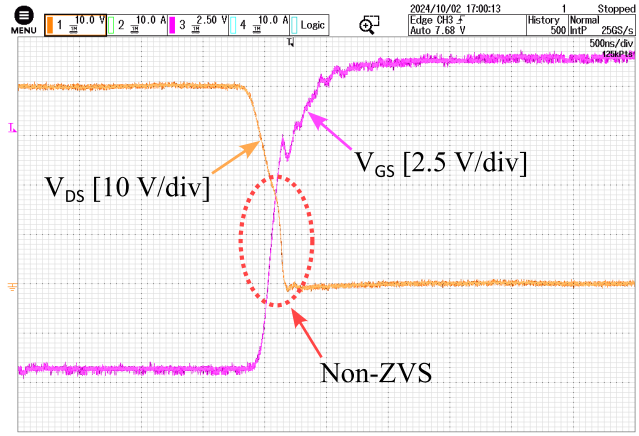

(c)

Fig. 17. Measurements of the turn-on transition of the drain–source voltage (V_{DS}) and gate–source voltage (V_{GS}) of the H-bridge inverter at different operating points in Fig. 16. (a) ZVS is achieved at operating point 1 where $\Sigma k = 0.3227 < \Sigma k_{crit} = (R_{Lac}/\omega_0 L_n^R) = 0.3495$. (b) ZVS is lost at operating point 2 where $\Sigma k = 0.3227 > \Sigma k_{crit} = (R_{Lac}/\omega_0 L_n^R) = 0.2595$. (c) ZVS is lost at operating point 3 where $\Sigma k = 0.3227 > \Sigma k_{crit} = (R_{Lac}/\omega_0 L_n^R) = 0.2151$.

by more than 3% similar to the aligned case. The measured circulating current obtained by the power analyzer is displayed in Fig. 12 for the aligned condition and in Fig. 13 for the misaligned condition. In both the figures, it can be observed that the total rms current of the improved compensation is closer to the sum of the rms currents of the individual modules, thus reducing the circulating currents. Finally, the waveforms of the improved compensation during both the aligned and misaligned conditions are presented in Figs. 14 and 15. The combined current waveform at the Rx side is displayed due to the limited available channels on the oscilloscope. Nevertheless, both the figures show that the system exhibits inductive behavior as the Tx currents lag behind U_{AB}. Furthermore, this indicates that the system is bifurcation-free. However, further measurements are necessary to fully verify this.

C. Bifurcation Verification

To demonstrate the validity of the proposed bifurcation guideline, the system described in Section IV-A will be operated under three different load conditions. The phase angles of the input impedance of these load conditions are depicted in Fig. 16. As anticipated, the system bifurcates when the output voltage reaches 30 or 25 V. According to (27) in Section III-B, the critical coupling of the system would decrease with a reduced load. To verify whether the system attains ZVS at these load conditions, the turn-on transition of the drain–source voltage (V_{DS}) and gate–source voltage (V_{GS}) of the H-bridge inverter are measured at the indicated operating points in Fig. 16.

The measurements are shown in Fig. 17. ZVS is maintained at operating point 1. This result agrees with Fig. 16 as operating point 1 operates in the inductive region. In contrast, ZVS is lost at operating points 2 and 3 as there is insufficient turn-off current to discharge the output capacitance of the MOSFET fully. These results also agree with Fig. 16 as both the operating points are in the capacitive region. The previous results validate the conclusions in Section III-B.

V. Conclusion

This article demonstrates an improved compensation tuning method and proposes a design guideline to mitigate bifurcation in multimodular IPT systems, aiming to enhance efficiency and ensure ZVS. The approach is based on closed-form equations to model the inter- and cross-coupling of a multimodular IPT system. The analytical model shows that the improved compensation tuning approach effectively compensates for the intercoupling introduced by multiple charging pads. Based on the analytical model of the multimodular IPT system, a critical sum of the coupling coefficients is derived, which provides a solution to a bifurcation-free design. The experimental results indicate that the improved compensation tuning method increases the power transfer efficiency by 2% under aligned conditions and 3% when misaligned, compared with the conventional compensation tuning method. Furthermore, the proposed bifurcation mitigation guideline has been validated using the experimental setup. Although this study focuses on a quadruple modular IPT system, the presented principles and guidelines are scalable to include more modules. These design approaches can serve as valuable guidelines for designing efficient and bifurcation-free multimodular IPT systems.

REFERENCES

[1] H. Feng, R. Tavakoli, O. C. Onar, and Z. Pantic, "Advances in high-power wireless charging systems: Overview and design considerations," *IEEE Trans. Transport. Electrific.*, vol. 6, no. 3, pp. 886–919, Sep. 2020.

[2] S. Y. Choi, S. Y. Jeong, B. W. Gu, G. C. Lim, and C. T. Rim, "Ultraslim S-type power supply rails for roadway-powered electric vehicles," *IEEE Trans. Power Electron.*, vol. 30, no. 11, pp. 6456–6468, Nov. 2015.

[3] M. Mohammad et al., "Bidirectional LCC–LCC-Compensated 20-kW wireless power transfer system for medium-duty vehicle charging," *IEEE Trans. Transport. Electrific.*, vol. 7, no. 3, pp. 1205–1218, Sep. 2021.

[4] B. Goeldi, J. Tritschler, and S. Reichert, "Measurement results of a 22 kW bidirectional inductive charger," in *Proc. PCIM Eur. ; Int. Exhib. Conf. Power Electron., Intell. Motion, Renew. Energy Energy Manage.*, May 2015, pp. 1–8.

[5] W. Shi et al., "Design of a highly efficient 20-kW inductive power transfer system with improved misalignment performance," *IEEE Trans. Transport. Electrific.*, vol. 8, no. 2, pp. 2384–2399, Jun. 2022.

[6] A. Calabro, B. Cohen, A. Daga, J. Miller, and F. McMahon, "Performance of 200-kW inductive charging system for range extension of electric transit buses," in *Proc. IEEE Transport. Electrific. Conf. Expo (ITEC)*, Jun. 2019, pp. 1–5.

[7] J. Shin et al., "Design and implementation of shaped magnetic-resonance-based wireless power transfer system for roadway-powered moving electric vehicles," *IEEE Trans. Ind. Electron.*, vol. 61, no. 3, pp. 1179–1192, Mar. 2014.

[8] J. H. Kim et al., "Development of 1-MW inductive power transfer system for a high-speed train," *IEEE Trans. Ind. Electron.*, vol. 62, no. 10, pp. 6242–6250, Oct. 2015.

[9] H. Hao, G. A. Covic, and J. T. Boys, "A parallel topology for inductive power transfer power supplies," *IEEE Trans. Power Electron.*, vol. 29, no. 3, pp. 1140–1151, Mar. 2014.

[10] T. Shijo, K. Ogawa, M. Suzuki, Y. Kanekiyo, M. Ishida, and S. Obayashi, "EMI reduction technology in 85 kHz band 44 kW wireless power transfer system for rapid contactless charging of electric bus," in *Proc. IEEE Energy Convers. Congr. Exposit. (ECCE)*, Sep. 2016, pp. 1–6.

[11] A. Hossain, P. Darvish, S. Mekhilef, K. S. Tey, and C. W. Tong, "A new coil structure of dual transmitters and dual receivers with integrated decoupling coils for increasing power transfer and misalignment tolerance of wireless EV charging system," *IEEE Trans. Ind. Electron.*, vol. 69, no. 8, pp. 7869–7878, Aug. 2022.

[12] H. Chen et al., "Modular four-channel 50 kW WPT system with decoupled coil design for fast EV charging," *IEEE Access*, vol. 9, pp. 136083–136093, 2021.

[13] Y. Li, R. Mai, L. Lu, T. Lin, Y. Liu, and Z. He, "Analysis and transmitter currents decomposition based control for multiple overlapped transmitters based WPT systems considering cross couplings," *IEEE Trans. Power Electron.*, vol. 33, no. 2, pp. 1829–1842, Feb. 2018.

[14] Y. Li, R. Mai, L. Ma, and Z. He, "Dual parallel wound primary coils based ipt systems and its power allocation technique," *Proc. CSEE*, vol. 35, no. 17, pp. 4454–4460, Jul. 2015.

[15] F. Lu, H. Zhang, H. Hofmann, and C. C. Mi, "A dynamic charging system with reduced output power pulsation for electric vehicles," *IEEE Trans. Ind. Electron.*, vol. 63, no. 10, pp. 6580–6590, Oct. 2016.

[16] Q.-T. Vo, Y. Sakamaki, Q.-T. Duong, and M. Okada, "Compensation of cross-coupling in MIMO inductive power transfer systems," *IEEE Access*, vol. 12, pp. 46995–47008, 2024.

[17] R. Mai, Y. Luo, B. Yang, Y. Song, S. Liu, and Z. He, "Decoupling circuit for automated guided vehicles IPT charging systems with dual receivers," *IEEE Trans. Power Electron.*, vol. 35, no. 7, pp. 6652–6657, Jul. 2020.

[18] Y. Luo, R. Mai, Y. Song, C. Zhu, and Z. He, "An inductive power transfer system with LCC-DDS topology to achieve magnetic field suppression and receiver lightweight," *IEEE Trans. Transport. Electrific.*, vol. 9, no. 1, pp. 1937–1949, Mar. 2023.

[19] K. Aditya and S. S. Williamson, "Design guidelines to avoid bifurcation in a series–series compensated inductive power transfer system," *IEEE Trans. Ind. Electron.*, vol. 66, no. 5, pp. 3973–3982, May 2019.

[20] C.-S. Wang, O. H. Stielau, and G. A. Covic, "Design considerations for a contactless electric vehicle battery charger," *IEEE Trans. Ind. Electron.*, vol. 52, no. 5, pp. 1308–1314, Oct. 2005.

[21] R. Narayanamoorthi, A. V. Juliet, and B. Chokkalingam, "Cross interference minimization and simultaneous wireless power transfer to multiple frequency loads using frequency bifurcation approach," *IEEE Trans. Power Electron.*, vol. 34, no. 11, pp. 10898–10909, Feb. 2019.

[22] R. Huang, B. Zhang, D. Qiu, and Y. Zhang, "Frequency splitting phenomena of magnetic resonant coupling wireless power transfer," *IEEE Trans. Magn.*, vol. 50, no. 11, pp. 1–4, 2014.

[23] U. Iruretagoyena, A. Garcia-Bediaga, L. Mir, H. Camblong, and I. Villar, "Bifurcation limits and non-idealities effects in a three-phase dynamic IPT system," *IEEE Trans. Power Electron.*, vol. 35, no. 1, pp. 208–219, Jan. 2020.

[24] V. Shevchenko, O. Husev, R. Strzelecki, B. Pakhaliuk, N. Poliakov, and N. Strzelecka, "Compensation topologies in IPT systems: Standards, requirements, classification, analysis, comparison and application," *IEEE Access*, vol. 7, pp. 120559–120580, 2019.

[25] W. Li, H. Zhao, J. Deng, S. Li, and C. C. Mi, "Comparison study on SS and double-sided LCC compensation topologies for EV/PHEV wireless chargers," *IEEE Trans. Veh. Technol.*, vol. 65, no. 6, pp. 4429–4439, Jun. 2016.

[26] R. L. Steigerwald, "A comparison of half-bridge resonant converter topologies," *IEEE Trans. Power Electron.*, vol. 3, no. 2, pp. 174–182, Apr. 1988.

Calvin Riekerk (Graduate Student Member, IEEE) received the B.S. and M.S. degrees in electrical engineering from Delft University of Technology (TU Delft), Delft, The Netherlands, in 2018 and 2020, respectively, where he is currently pursuing the Ph.D. degree in wireless power transfer.

He is a System Engineer with Nederlandse Spoorwegen (NS). His research interests include power electronics and wireless charging.

Jianning Dong (Senior Member, IEEE) received the B.Sc. and Ph.D. degrees in electrical engineering from Southeast University, Nanjing, China, in 2010 and 2015, respectively.

In 2016, he worked at the McMaster Automotive Resource Centre, McMaster University, Hamilton, ON, Canada, as a Post-Doctoral Researcher. Since October 2016, he has been an Assistant Professor, and then from 2025 an Associate Professor with the DC Systems, Energy Conversion and Storage (DCE&S) Group, Delft University of Technology, Delft, The Netherlands. His research interests include electromechanical energy conversion and contactless power transfer, through which he applies knowledge to applications such as transportation electrification and renewable energy generation/utilization.

Pavol Bauer (Senior Member, IEEE) is currently a Full Professor with the Department of Electrical Sustainable Energy, Delft University of Technology, Delft, The Netherlands, and the Head of the DC Systems, Energy Conversion and Storage Group. From 2002 to 2003, he was working partially at KEMA (DNV GL), Arnhem, The Netherlands, on different projects related to power electronics applications in power systems. He published more than 180 journal articles and more than 500 conference papers in his field (with 65 H factor Google scholar and 43 Web of Science), and he is an author or co-author of eight books and holds ten international patents and organized several tutorials at the international conferences. He has worked on many projects for industry concerning wind and wave energy, power electronic applications for power systems such as Smarttrafo; HVDC systems, projects for smart cities such as PV charging of electric vehicles, PV and storage integration, and contactless charging; and he participated in several Leonardo da Vinci, H2020 and Electric Mobility Europe EU projects as project partner (ELINA, INETELE, E-Pragmatic, Micact, Trolley 2.0, OSCD, P2P, Progressus, Tulip, Flow) and a coordinator (PEMCWebLab.com-Edipe, SustEner, Eranet DCMICRO). His main research interests include power electronics for charging of electric vehicles and DC grids.

Dr. Bauer is a member of the Executive Committee of European Power Electronics Association (EPE) and a member of the International Steering Committee at numerous conferences. He is a former Chair of the Benelux IEEE Joint Industry Applications Society, Power Electronics and Power Engineering Society Chapter, the Chair of the Power Electronics and Motion Control (PEMC) Council, and the Chair of the Benelux IEEE Industrial Electronics chapter.